remote sensing

MDPI

Article

Evaluating Water Controls on Vegetation Growth in the Semi-Arid Sahel Using Field and Earth Observation Data

Abdulhakim M. Abdi [1,*], Niklas Boke-Olén [1], David E. Tenenbaum [1], Torbern Tagesson [2], Bernard Cappelaere [3] and Jonas Ardö [1]

1 Department of Physical Geography and Ecosystem Science, Lund University, Sölvegatan 12, 22362 Lund, Sweden; niklas.boke-olen@nateko.lu.se (N.B.-O.); david.tenenbaum@nateko.lu.se (D.E.T.); jonas.ardo@nateko.lu.se (J.A.)

2 Department of Geosciences and Natural Resource Management, University of Copenhagen, DK-1350 Copenhagen, Denmark; torbern.tagesson@ign.ku.dk

3 HydroSciences Montpellier, IRD, CNRS, University Montpellier, 34090 Montpellier, France; bernard.cappelaere@ird.fr

* Correspondence: hakim.abdi@gmail.com; Tel.: +46-46-222-3132

Academic Editors: John S. Kimball, Kaiyu Guan, Jose Moreno and Prasad S. Thenkabail
Received: 31 January 2017; Accepted: 14 March 2017; Published: 21 March 2017

Abstract: Water loss is a crucial factor for vegetation in the semi-arid Sahel region of Africa. Global satellite-driven estimates of plant CO_2 uptake (gross primary productivity, GPP) have been found to not accurately account for Sahelian conditions, particularly the impact of canopy water stress. Here, we identify the main biophysical limitations that induce canopy water stress in Sahelian vegetation and evaluate the relationships between field data and Earth observation-derived spectral products for up-scaling GPP. We find that plant-available water and vapor pressure deficit together control the GPP of Sahelian vegetation through their impact on the greening and browning phases. Our results show that a multiple linear regression (MLR) GPP model that combines the enhanced vegetation index, land surface temperature, and the short-wave infrared reflectance (Band 7, 2105–2155 nm) of the moderate-resolution imaging spectroradiometer satellite sensor was able to explain between 88% and 96% of the variability of eddy covariance flux tower GPP at three Sahelian sites (overall = 89%). The MLR GPP model presented here is potentially scalable at a relatively high spatial and temporal resolution. Given the scarcity of field data on CO_2 fluxes in the Sahel, this scalability is important due to the low number of flux towers in the region.

Keywords: Sahel; drought; gross primary productivity; Earth observation; plant-available water; soil moisture; vapor pressure deficit; plant stress; greening; browning

1. Introduction

The Sahel is an arid and semi-arid region that stretches from the Atlantic Ocean in the west to the Red Sea in the east and separates the hyper-arid Sahara desert from the sub-humid and humid regions to the south (Figure 1). The Sahel has experienced a prolonged dry period from the mid-1960s through the late 1980s in which there were severe droughts that resulted in humanitarian crises [1]. Recovery from this dry period was reported by Eklundh and Olsson [2], who observed strong increases in seasonal satellite-derived normalized difference vegetation index (NDVI) from the mid-1980s onwards. This increase in vegetation greenness began to be referred to as the "greening of the Sahel" [3], and is the result of increases in both herbaceous [4] and tree cover [5]. Seaquist et al. [6] translated this greening into sequestered carbon (C) and found that 51 megatonnes of C (MtC) per year where taken up by Sahelian vegetation between 1982 and 1999 resulting in a net increase of 918 MtC

over the 18-year period. The key suggested mechanism behind the greening is increased rainfall [7], and to a lesser extent, improved land use and migration-induced land abandonment [3].

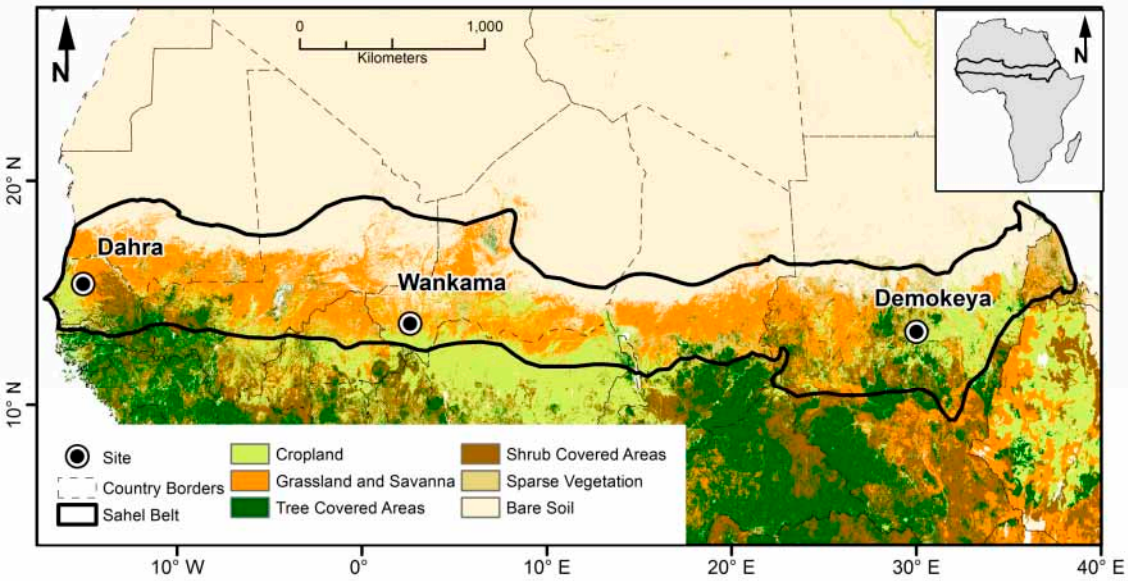

Figure 1. The location of the sites and the dominant land cover classes in Sahel. The Sahelian borders are based on the 150- and 700-mm annual rainfall isohyets. Dominant land cover types are according to the Food and Agriculture Organization's 2014 Global Land Cover-SHARE database. Grassland and croplands together cover more than 67% of the total surface area of the Sahel.

Gross primary productivity (GPP) is the total amount of C plant extract from the atmosphere through photosynthesis. Some of this C goes to maintaining plant tissue, and is thus lost through autotrophic respiration (Ra). The remaining C is stored as phytomass (net primary productivity, NPP = GPP − Ra). The capacity of Sahelian ecosystems to provide essential food, fuel, feed and fiber is a function of available NPP [8]. Since these ecosystem services are essential, evaluating the environmental controls that modulate GPP dynamics is necessary for accurate accounting of primary productivity. The Sahel has a single growing season that starts in July and ends in October [9] with considerable inter-annual variability in the spatial distribution and quantity of rainfall [10,11]. The driest parts of the northern Sahel receive an annual average of 150 mm of rain, while the southern parts receive an annual average of ~750 mm [12] (Figure 1).

The Sahel (Figure 1) is dominated by plants that have the C_4 photosynthetic pathway [13], which are adapted to warm, arid environments and are composed mainly of grasses, herbs and crops. The mean tree canopy cover is approximately 7.3% and comprises trees that use the C_3 photosynthetic pathway [14,15]. It is well known that moisture availability controls C fluxes in drylands such as the Sahel, and several studies have attempted to explain the underlying mechanisms of its modulation of primary productivity in these regions [7,16–21]. Merbold et al. [22] found that mean annual rainfall is strongly correlated with maximum photosynthetic capacity and is the predominant factor driving C fluxes across Africa. With rainfall, the greening phase commences (Figure 2), and soil moisture is replenished, which impacts the amount of energy partitioned into evapotranspiration [21,23,24]. Rainfall also increases humidity, which lowers the difference between the vapor pressure deficit inside the leaf and that of the air. This difference in vapor pressure deficit was found to be a key factor affecting stomatal conductance of Sahelian plants [25,26]. The browning phase (Figure 2) begins with a decrease in soil moisture and increase in both surface temperature and vapor pressure deficit, which triggers the closure of the stomata to prevent water loss through transpiration. The closure of the stomata prohibits the flow of CO_2 into the leaf and thus reduces GPP.

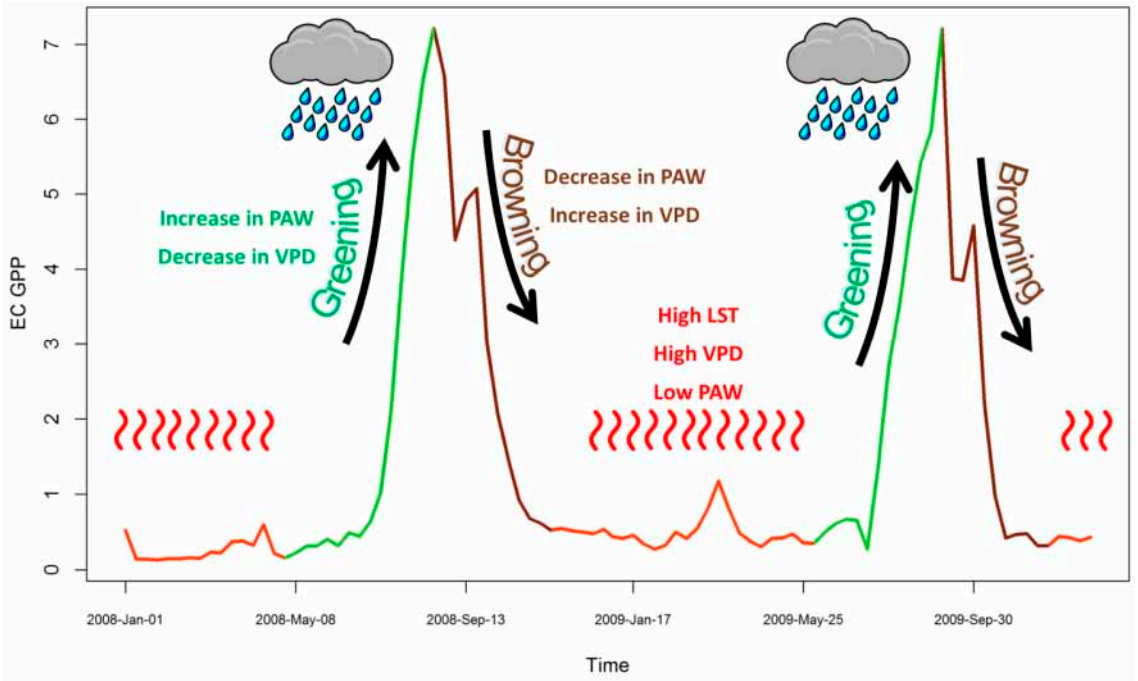

Figure 2. Conceptual diagram of the greening and browning processes present in the Sahel. The two peaks represent the uptake of CO_2 and the increase in gross primary productivity (GPP). The greening phase begins with the start of the rainy season and the increase in plant-available water (PAW, Section 3.3.1). During the greening phase vapor pressure deficit (VPD, Section 3.3.2) decreases and so does land surface temperature (LST). The beginning of the browning phase starts with a reduction in PAW and increase in VPD and LST.

Most studies covering the Sahel base their results on a handful of sites, due to the scarcity of data on C fluxes over the region's 3.3 million km^2 of surface area [27]. Thus, Earth observation is an important tool for large-scale studies of the GPP of Sahelian ecosystems. The only global model of satellite-driven GPP estimates is the MOD17 production efficiency model [28], which is based on the light-use efficiency concept [29]. However, this dataset has been shown to considerably underestimate GPP over semi-arid Sahelian ecosystems [21,30]. Recent work by Sadeghi et al. [31] found that the shortwave infrared spectral range of 2105–2155 nm, corresponding to band 7 in the moderate-resolution imaging spectroradiometer (MODIS) satellite sensor, provides optimal sensitivity to variations in soil moisture. Furthermore, aerosol effects are negligible because most aerosol particulates are smaller than that wavelength range [32]. The drying and wetting processes that influence vegetative growth could be captured by satellite sensors that cover this spectral range because soil moisture at the top 1–2 cm of soil significantly influences soil surface reflectance at these wavelengths [33,34]. Another recent study by Tian and Philpot [35] found that shortwave infrared radiation within the spectral range of 1850–2130 nm was sensitive to soil volumetric water content. Consequently, there is potential utility of this spectral range in C cycle studies that focus on Sahelian settings. This study has two objectives: (1) To identify the relative strengths of biophysical limitations that reduce CO_2 uptake in the Sahel; and (2) evaluate empirical relationships between Earth observation-derived spectral products that can account for these limitations to better explain the variability in eddy covariance (EC) GPP using Earth observation data.

2. Field Sites

We used three eddy covariance sites located in Sudan, Niger and Senegal. All three sites are within a narrow latitudinal band between 13°N and 15°N (Figure 1). A summary of the sites is presented below and summarized in Table 1.

Table 1. Basic site characteristics including location in decimal degrees (DD), vegetation and soil types, mean annual precipitation (MAP), and mean annual air temperature at 2-m height (MAT). The DS and GS in the relative humidity column refer to Dry Season (November–June) and Growing Season (July–October), respectively.

Site, Country	Longitude, Latitude (DD)	Vegetation Type	Soil Type	MAP (mm)	MAT (°C)	Measurement Years	Rel. Hum. DS/GS (%)	Ref.
Demokeya, Sudan	30.47, 13.28	Sparse acacia savanna	Cambic Arenosols	320	30	2007–2009	16/57	[36]
Wankama, Niger	2.63, 13.64	Fallow shrubland	Sandy Ferruginous Arenosols	479	30	2005–2009	28/75	[37]
Dahra, Senegal	−15.43, 15.40	Open woody savanna	Luvic Arenosols	416	29	2010–2013	9/63	[38]

2.1. Demokeya, Sudan

Demokeya (13.282°N, 30.478°E) is located in the North Kordofan state. Mean annual air temperature is 30 °C and mean annual precipitation is 320 mm (Table 1). The landscape around the site is a typical Sahelian savanna, comprised of sparse trees, mainly *Acacia senegal* and *Acacia nilotica*, with a canopy cover of approximately 7%. The ground cover comprises annual grasses, primarily *Cenchrus biflorus*, *Eragrostis tremula*, and *Aristida pallida*. The sandy soils are poor in nutrients, have low soil organic C, and low cation exchange capacity [39]. A complete description of Demokeya is provided in Ardö et al. [36].

2.2. Wankama, Niger

The Wankama site is divided into two sub-sites, Wankama Millet (13.644°N, 2.629°E) and Wankama Fallow (13.647°N, 2.633°E), both of which are located in southwest Niger and within close proximity to each other. Mean annual air temperature is 30 °C and mean annual precipitation is 479 mm (Table 1). Only the fallow site has been used in this study. This site is composed of shrub and herbaceous layers; the shrub layer is primarily composed of *Guiera senegalensis* and the herbaceous layer is dominated by *Zornia glochidiata* [40]. The soils are mostly sandy with low nitrogen and phosphate content. A complete description of Wankama is provided in Cappelaere et al. [37].

2.3. Dahra, Senegal

Dahra (15.402°N, 15.432°W) is located in the Louga province of northern Senegal. Long-term mean annual air temperature is 29 °C and mean annual precipitation is 416 mm (Table 1). The vegetation around the site is grazed by livestock and dominated by annual grasses, particularly *Aristida adscensionis*, *Zornia latifolia*, *Eragrostis tremula*, *Dactyloctenium aegyptium*, and *Cenchrus biflorus*. The canopy cover is approximately 3% and comprises *Acacia Senegal*, *Acacia tortilis*, and *Balanites aegyptiaca*. The soils are sandy with low water holding capacity and organic matter content. A complete description of Dahra is provided in Tagesson et al. [38].

3. Data and Methods

3.1. Field Data

3.1.1. Eddy Covariance Gross Primary Productivity

The eddy covariance (EC) systems at all three sites are equipped with LI7500 open path infrared CO_2/H_2O analyzers (LI–COR Inc., Lincoln, NE, USA) and GILL R3 triple-axis sonic anemometers (GILL Instruments, Lymington, UK). Eddy covariance data were recorded at 20 Hz and averaged over 30-min periods. The EC method measures net ecosystem exchange of CO_2 (NEE) and following the approach in Tagesson et al. [41], NEE was partitioned into GPP and ecosystem respiration (R_{eco})

using a non-linear asymptotic regression with incoming photosynthetically active radiation and vapor pressure deficit as independent variables. Gaps in the time series of NEE, GPP and R_{eco} were consequently gap-filled, again following the method outlined in Tagesson et al. [41].

3.1.2. Climatic Variables

Air temperature (°C) and relative humidity (%) at 2 m were monitored using MP100A Temperature and Relative Humidity Probe (Rotronic) in Demokeya, with Vaisala HMP45C probes (Vaisala Oyj, Helsinki, Finland) in Wankama, and Campbell CS215 (Campbell Scientific, Logan, UT, USA) in Dahra. Precipitation (mm) was recorded using ARG100 tipping buckets (Campbell Scientific, UT, USA) at all three sites. Volumetric soil moisture was recorded using CS616 water content reflectometers (Campbell Scientific) in Demokeya and Wankama, and HH2 probe (Delta T Devices) in Dahra. These parameters were recorded every 10–30 s and averaged for every 30 min. Measurement depths varied with site and were dependent on the field campaign. Volumetric soil moisture was summed from top of soil to 50 cm depth in Dahra and Wankama, and to 60 cm depth in Demokeya in order to compute plant-available water (see Section 3.3.1).

3.2. Earth Observation Data

The moderate-resolution imaging spectroradiometer (MODIS) sensor on board NASA's Terra and Aqua satellites has a viewing swath width of 2330 km and images the entire surface of the Earth every one to two days. The MCD43A4 nadir bidirectional reflectance distribution function adjusted reflectance (NBAR) product, which is produced every 8 days within 16 days of acquisition, is preferable over the other surface reflectance products (MOD09A1/MYD09A1) because it is adjusted using a bidirectional reflectance distribution function to model at-nadir values [42]. The Collection 5.1 MCD43A4 NBAR Level 3 and MOD17 8-day GPP product (MOD17A2) products were downloaded for each site from the Oak Ridge National Laboratory Distributed Active Archive Center (ORNL-DAAC, daac.ornl.gov/modisglobal). Band 7 of the MCD43A4 NBAR product (henceforth, MODIS NBAR Band 7 or simply Band 7) covers the shortwave infrared wavelength range of 2105–2155 nm that is crucial for capturing sensitivity to variations in soil moisture [31]. These data are provided as ASCII files containing observations within a specified radius around a particular point of interest. We selected a 3 × 3 km area around each flux tower site based on footprint analysis conducted in Demokeya by Sjöström et al. [43] and in Dahra by Tagesson et al. [44]. Land surface temperature (LST) has been found to strongly influence ecosystem respiration [45,46] and has been used estimate vapor pressure deficit [47]. Sims et al. [48] used LST to characterize temperature and drought stress in a modeling framework that used MODIS-enhanced vegetation index (EVI) as a predictor of GPP. In order to test the applicability of LST for improving GPP modeling, we downloaded the 8-day MOD11A2/MYD11A2 Level 3 LST product (Collection 5.1) from the ORNL-DAAC database (daac.ornl.gov/modisglobal).

3.3. Methodology

This section details the techniques that were used to derive three field-based variables: plant-available water, vapor pressure deficit and the antecedent precipitation index, and one Earth observation-based variable: the enhanced vegetation index. The rationale behind the selection of each variable is also described. Finally, the statistical methods that were chosen to construct and evaluate the models are detailed in the concluding subsection.

3.3.1. Plant-Available Water

Plant-available water (PAW) is the amount of water present in the soil that can be extracted by roots. PAW is a function of soil type, soil water content at field capacity (moisture left over after percolation) and permanent wilting point (soil moisture that is unavailable to plants). It is an important

parameter in the terrestrial water cycle and may have a considerable influence on GPP [49]. PAW was calculated as:

$$PAW = (SWC - PWP) \times D \quad (1)$$

where *PAW* is plant-available water (mm); *SWC* is volumetric soil water content at field capacity (m^3 m^{-3}); *PWP* is the soil texture-dependent permanent wilting point from Table 2 expressed as a dimensionless fraction (m^3 m^{-3}); and *D* is the depth (mm) at which the soil moisture measurements were made. The PWP is a biophysical parameter that quantifies the condition where the force exerted by a plant to remove water from the soil (−1500 kPa) is countered by the forces binding the water to the soil [50]. At this point plant roots cannot extract further water from the soil and sustain growth, thus leading to wilting.

Table 2. Field capacity, soil texture and permanent wilting point (PWP) at the three sites. Soil texture was included with the soil moisture data provided by the International Soil Monitoring Network (ISMN) [51]. This information was verified against site descriptions provided by the principal investigator at each site. Field capacity and PWP was derived from the Africa Soil Profiles Database (v1.2) [52] based on the soil texture configuration at each site.

Site	Field Capacity, %	Soil Texture, % (Sand/Silt/Clay)		Permanent Wilting Point, %	
		0–30 cm	30–100 cm	0–30 cm	30–100 cm
Demokeya	15	89/6/5	90/5/5	2	3
Wankama Fallow	16	90/5/5	88/5/7	3	3
Dahra	7	89/6/5	89/5/6	2	4

3.3.2. Vapor Pressure Deficit

When plants transpire, the mixture of air and water exiting the stomata is saturated at a relative humidity of ~100% [53]. The maximum amount of water vapor the air can hold at a particular temperature is a function of the temperature itself, so there is potential for higher transpiration at higher temperatures. The climate of the Sahel is generally hot, with a mean annual air temperature of 30 °C across the three sites. The average relative humidity (RH) across the three sites is 18% in the dry season and 65% in the growing season according to the field measurements. Vapor pressure deficit (VPD) [54] is the difference between the amount of water in the air and the maximum amount of water the air can hold when it is saturated, and is a limiting factor for Sahelian GPP [25,26,55]. VPD was calculated from field-measured air temperature (T_a, °C) and relative humidity (RH, %) following the approach described in Ward et al. [56]:

$$e_s = 0.611 \times \exp\left[17.27 \times \frac{T_a}{T_a + 237.3}\right] \quad (2)$$

where e_s is the saturation vapor pressure (kPa) at a certain T_a. Then, the actual vapor pressure (e_a, kPa) is calculated from RH and e_s:

$$e_a = \left(\frac{RH}{100}\right) \times e_s \quad (3)$$

Finally, VPD (kPa) is estimated as the difference between the two:

$$VPD = e_s - e_a \quad (4)$$

3.3.3. Antecedent Precipitation Index

The timing, quantity and effects of previous rainfall on vegetation are important because it takes time for water to percolate through soil and become available for plants. When precipitation occurs, soil moisture conditions evolve as a function of its current degree of saturation. Antecedent precipitation

index (API) [57] has been previously used to characterize the influence of past rainfall events on vegetation [58]. The formulation of API used here follows Heggen [59]:

$$API = \sum_{P \geq 1}^{n=8} P_t k^{-a} \quad (5)$$

where API is the antecedent precipitation index in mm per 8 days; P_t is the observed precipitation amount on period t; the decay constant, k, ranges between 0.80 and 0.98 [60] and a value of 0.90 has been applied in this study; a is the number of antecedent days.

3.3.4. Enhanced Vegetation Index

The Enhanced Vegetation Index (EVI) [61,62] utilizes three spectral bands that summarize radiometric and biophysical vegetation characteristics. EVI includes the blue band in addition to the vegetation-sensitive red and near-infrared bands. A set of coefficients and the blue band enhances the vegetation signal by reducing the influence of soil reflectance and atmospheric scattering. Sjöström et al. [21] and Ma et al. [63] found that EVI follows the seasonal dynamics of EC GPP better than the MODIS-derived GPP in Sahelian and Australian xeric savannas, respectively.

$$EVI = 2.5 \times \frac{NIR - RED}{NIR + 6 \times RED - 7.5 \times BLUE + 1} \quad (6)$$

where *RED*, *NIR* and *BLUE* represent MCD43A4 NBAR Level 3 surface reflectance acquired in the red (620–670 nm), near infrared (841–876 nm) and blue (459–479 nm) portions of the electromagnetic spectrum, respectively.

3.3.5. Statistical Analysis

Data processing, statistical analysis and visualization were performed in R 3.1.1 (www.r-project.org). Both linear and multiple linear regression (MLR) were used to examine the relationships between VPD, PAW, LST, EVI, NBAR Band 7, and EC GPP. The relationships were used to build GPP models composed of field metrics of water stress and vegetation indices as input data. Additionally partial correlations were performed on both the field and Earth-observation variables during the greening and browning phases using Spearman's rank order correlation [64]. This was done to assess the relationship of each variable with EC GPP while keeping the influence of the other variables constant. Within each year, the greening phase was delineated as the period from the lowest to the highest GPP value, and the browning was delineated as the following period from maximum GPP to its lowest value. The coefficient of determination (R^2) was calculated as a measure of the amount of EC GPP variance explained by each set of predictor variables. Bayesian information criterion (BIC) [65] was chosen to identify the model which best describes the EC GPP data:

$$BIC = -2\ln(L) + q\ln(n) \quad (7)$$

where L is the maximum value of the likelihood function of the model, q is the total number of parameters and n is the number of sample points. BIC considers both the goodness of fit and the number of parameters that achieve a certain degree of fit by levying a penalty term $q\ln(n)$ on increasing the number of parameters to prevent over-fitting. Root-mean-square error (RMSE) was calculated to evaluate the performance of each model output relative to EC GPP. RMSE calculates the square root of the variance and smaller values denote better model performance. An RMSE of 0.0 indicates perfect simulation of the EC GPP data.

$$RMSE = \sqrt{\frac{\sum_{t=1}^{n} (OBS - PRED)^2}{n}} \quad (8)$$

where *PRED* is the model-estimated GPP (g C m^{-2} d^{-1}), *OBS* is the EC GPP (g C m^{-2} d^{-1}), and *n* is the number of sample points.

4. Results and Discussion

4.1. Seasonal Dynamics and Inter-Annual Variability of EC GPP, PAW, VPD and API

Growing season average EC GPP was highest in Dahra at 8.6 g C m^{-2} d^{-1}, followed by Demokeya at 3.9 g C m^{-2} d^{-1} and Wankama Fallow with 3.5 g C m^{-2} d^{-1}. EC GPP was tightly coupled with climate across all sites (Figure 3). The greening phase was dominated by a rapid decrease in VPD and an increase in the amount of PAW. Growing season EC GPP was attained across all sites when PAW was generally above 25 mm (~0.04 m^3 m^{-3}) and when VPD was below 2 kPa, which is comparable to studies conducted in similar environments [22,66]. The decline in PAW and the onset of high VPD during times of drought reduces plant photosynthetic capacity by causing closure of stomata to prevent moisture loss [67]. Thus, a decrease in moisture during the growing season, as happened in Dahra in 2011, where there was 42% decrease in rainfall and 46% decrease in soil moisture from the previous year, could cause a reduction in GPP. Indeed, EC GPP in Dahra during the 2011 growing season was 72% less than the previous year. A similar pattern of decline was observed in Demokeya during the 2009 growing season when there was a 25% decrease in rainfall, 14% decrease in soil moisture, and a 9% decrease in GPP from the previous year (Figure 3a). When rainfall resumes to previous levels, as happened in 2012 in Dahra (Figure 3c), the herbaceous vegetation respond rapidly to changes in the soil water regime resulting in increased C uptake [13]. It has been shown that the terrestrial biosphere can retain "memory" of past wet or dry conditions through soil moisture or the vegetation itself [68,69]. In this study, the observed speed of vegetation response to the resumption of rainfall could be due to this land memory effect.

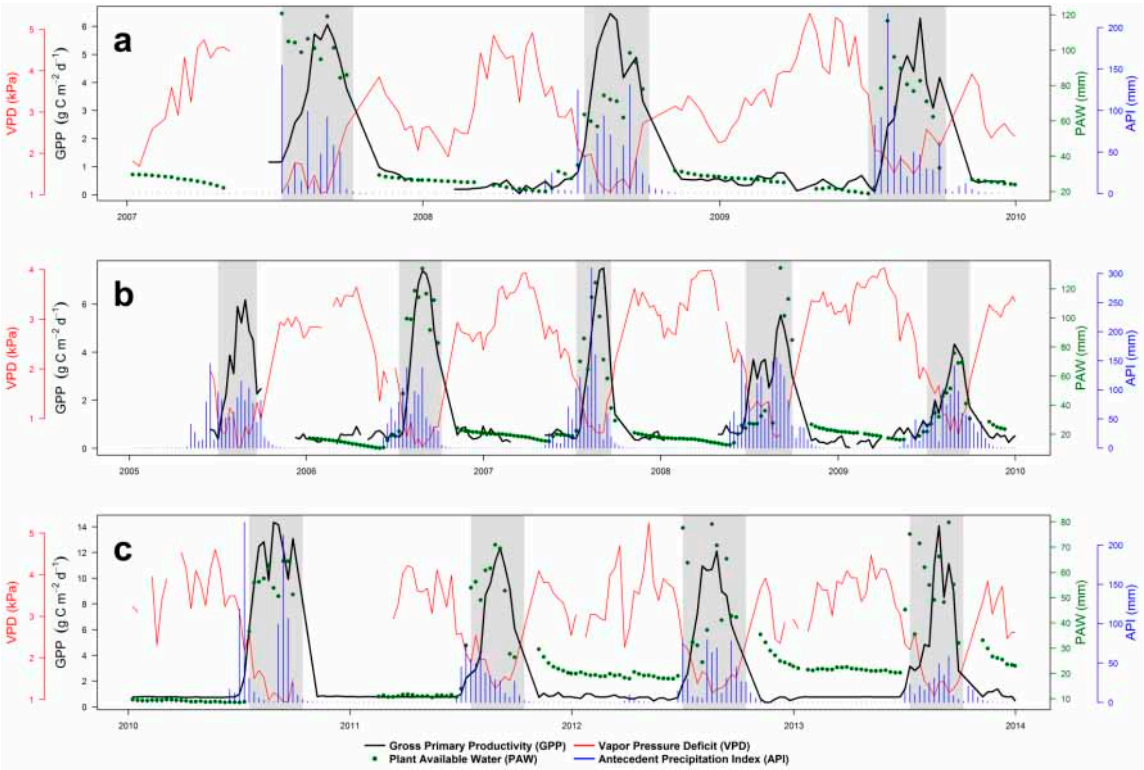

Figure 3. Site-level 8-day data for surface and subsurface conditions in (**a**) Demokeya; (**b**) Wankama Fallow; (**c**) Dahra. The shading indicates the growing season (July–October).

The seasonal variability of the field parameters, PAW, VPD and EC GPP, was fairly consistent across all sites (Figure 3). However, Dahra had the highest average EC GPP during the growing season (8.6 g C m^{-2} d^{-1}) despite having similar climatic and subsurface conditions as the other two sites (Table 1). A recent study by Tagesson et al. [70] provided two plausible reasons for the higher photosynthetic capacity at Dahra: (1) A total of 80% of the vegetative cover at Dahra is comprised of herbaceous C_4 plants, signifying a higher concentration of plants that are more productive under optimal climatic conditions (i.e., during the growing season); and (2) intense grazing disturbance causes plants to develop strategies that allocate more C to leaves thereby increasing their leaf area index and leading to increase in absorbed photosynthetically active radiation and C assimilation. A third plausible reason for the high EC GPP at Dahra is linked to the increase in relative humidity which ranges from 9% in the dry season to 63% in the growing season (Table 1). This is connected to the movement of the inter-tropical convergence zone (ITCZ) and the West African Monsoon, which transports moist air from the Gulf of Guinea to West Africa [13,38,71]. This large influx of humid air could allow the stomata to remain open longer during the growing season, thus enabling enhanced C uptake without increased water loss through transpiration. Growing season (July–October) API in Dahra was 153% higher than Demokeya and 57% higher than Wankama Fallow, and had higher intra-seasonal variability (standard deviation = 171%). This is also probably due to West African Monsoon, which causes higher amounts of rainfall at Dahra [71–74].

4.2. Relationship between EC GPP, PAW, VPD, and API

Cross-site relationships of PAW and VPD with EC GPP were fairly moderate (R^2 = 0.36 and 0.43, respectively). The relationships at the individual sites were varied with R^2 values of VPD ranging between 0.59 and 0.75 and those of PAW between 0.59 and 0.76 (Table 3). API was the worst-performing variable, averaging a cross-site R^2 of 0.33. This is probably due to the fact that rain events during the growing season were sporadic and API could not capture the lag effect each event had on EC GPP. The combination of PAW and VPD explained the largest variance across all three sites (R^2 = 0.47, RMSE = 2.06 g C m^{-2} d^{-1}), with the highest R^2 and lowest RMSE at Wankama Fallow (R^2 = 0.83, RMSE = 0.77 g C m^{-2} d^{-1}) (Table 3).

An overview of the relationship between EC GPP, VPD and PAW across all sites is shown in Figure 4. The dry season is characterized by high VPD (>2 kPa), which is linked to the reduction in evapotranspiration due to low PAW. With the reduction/closure of stomatal conductance, plants deactivate metabolic activity in the shoots to reduce consumption of water (and subsequent transpiration) while simultaneously enhancing uptake of water and nutrients by the roots to mitigate the effect of the dry season [75]. In the wetter savanna systems of the humid region (>750 mm of mean annual precipitation, MAP), it has been shown that a considerable amount of C is stored in the roots at the start of the dry season and is subsequently used by the herbaceous vegetation to re-sprout at the start of the next growing season [76]. If the dry season is intense, prolonged, or both, this memory effect allows vegetation to tap into these C reserves and maintain root respiration [77]. A recent global study by Murray-Tortarolo et al. [78] lends support to this, finding that the intensity and duration of the dry season has a larger impact on annual primary productivity than increased rainfall in the rainy season. Thus, a similar mechanism may take place in the poorer soils of the Sahel, where the herbaceous species are specialized to grow quickly at the beginning of the rainy season [13]. These subsurface mechanisms can in turn be influenced by anthropogenic activity as soil moisture amount and availability are influenced by land management practices [36,79].

When the rainy season commences, not only is soil water replenished and root water uptake increased, but VPD is reduced due to humid air masses from the northward movement of the ITCZ. In Wankama Fallow, maximum EC GPP is reached when PAW is greater than 125 mm and VPD is below 1.5 kPa, while in Demokeya maximum EC GPP occurs when PAW is above 90 mm and VPD is below 2 kPa. At Dahra, maximum EC GPP was reached at VPD levels similar to Demokeya and Wankama Fallow, however, PAW was relatively low compared to the other two sites at ~60 mm. The partial

correlation analysis revealed that the increase in C uptake during the greening phase, shortly after the onset of the first rains, is governed by the availability of PAW and a reduction in VPD (Table 4). The increase in soil moisture also decreases LST (Spearman's Rho, $r_s = -0.28$) due to evaporative cooling. These are further illustrated by scatterplot in Figure 5. The browning phase is characterized by a steep decrease in GPP and a reduction in PAW due to a cessation of the rains. The relationship of EC GPP, VPD and PAW were generally strong during both the greening and browning phases (Figure 5). The mechanism by which VPD and PAW interact is further illustrated in Figure 6, which uses the 2009 growing season in Demokeya as an example. The first rains occurred on July 4, however, the relative humidity began to increase from a mean of 15% in April and May, which is typical of the dry season, to 32% in June. Between 4 July and 1 September (the larger shaded area in Figure 6), the mean relative humidity was 64%. The effect of the increase in relative humidity, and decrease in VPD, a full month before the first rains is particularly interesting. This can play the role of an anticipatory mechanism for vegetation that enables it to begin photosynthesis rapidly at, or shortly before, the onset of rain [80]. The second GPP peak (smaller shaded area in Figure 6) can be explained by the second, smaller, rainfall event of that year, which was not sufficient enough to replenish PAW to previous levels. However, it created enough reduction in VPD that stimulated the vegetation to resume C assimilation (Figure 6).

Table 3. Summary of the regression analysis between eddy covariance gross primary productivity (EC GPP) and three field-measured water stress controls: plant-available water (PAW), vapor pressure deficit (VPD) and antecedent precipitation index (API) for each site. Also shown are the root-mean-square error (RMSE) and Bayesian information criterion (BIC) for each model.

Response = EC GPP		**Statistics**		
Demokeya	**RMSE**	**R^2**	***n***	**BIC**
API	1.61	0.28	97	382.04
VPD	1.22	0.59	95	321.88
PAW	1.19	0.62	89	298.27
VPD + API	1.22	0.59	95	326.36
API + PAW	1.19	0.62	89	301.82
PAW + VPD	1.12	0.66	89	291.87
Wankama Fallow	**RMSE**	**R^2**	***n***	**BIC**
API	1.54	0.33	159	605.44
VPD	0.96	0.74	157	448.70
PAW	0.91	0.76	132	365.07
VPD + API	0.94	0.75	156	445.64
API + PAW	0.91	0.77	131	366.92
PAW + VPD	0.77	0.83	129	318.23
Dahra	**RMSE**	**R^2**	***n***	**BIC**
API	2.91	0.38	161	815.93
PAW	2.51	0.59	154	736.34
VPD	1.99	0.75	146	631.43
API + PAW	2.28	0.64	147	680.49
VPD + API	1.92	0.77	146	624.80
VPD + PAW	1.88	0.77	139	590.21
All Sites	**RMSE**	**R^2**	***n***	**BIC**
API	2.37	0.33	417	1888.05
PAW	2.27	0.36	375	1780.69
VPD	2.21	0.43	398	1779.50
VPD + API	2.22	0.44	390	1697.36
API + PAW	2.18	0.45	367	1652.43
PAW + VPD	2.06	0.47	364	1624.53

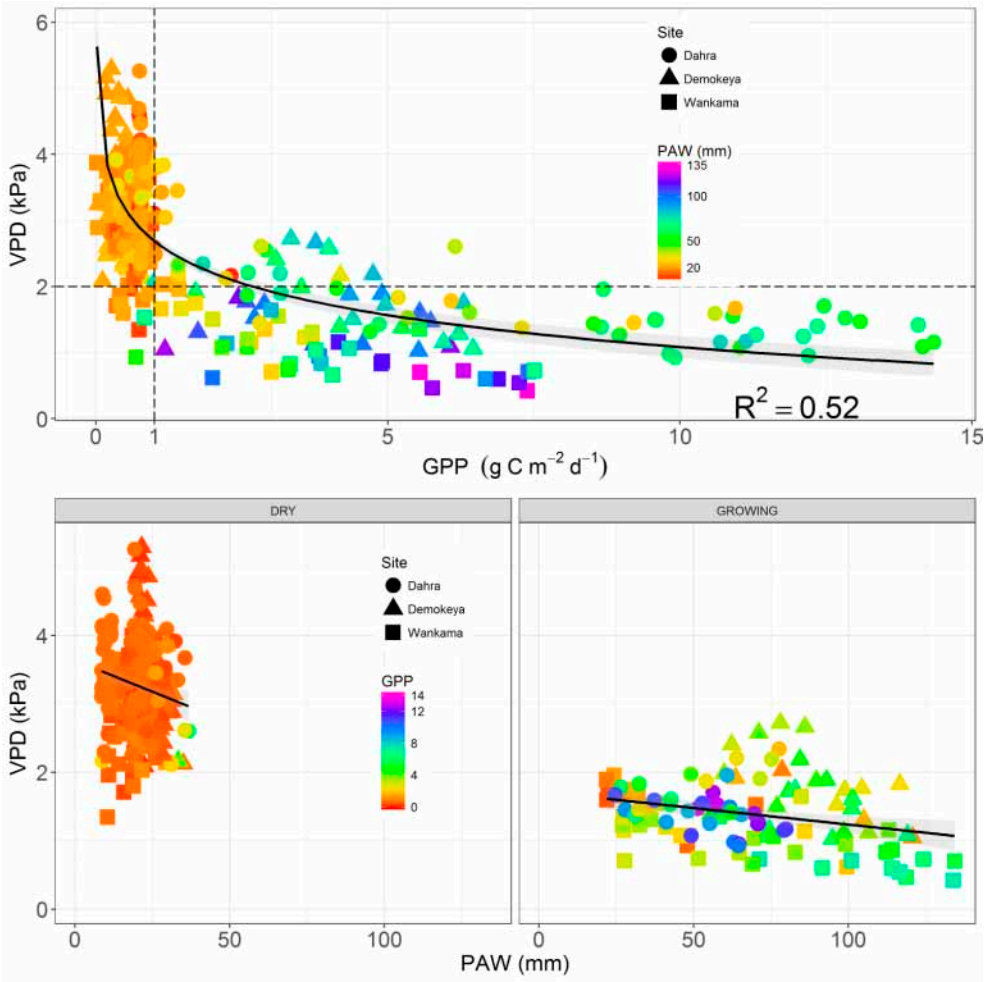

Figure 4. Top: Comparison of VPD and EC GPP, with coloring that indicates corresponding values of PAW for each site. Values to the left of the vertical dotted line (GPP < 1 g C m^{-2} d^{-1}) and above the horizontal dotted line (VPD > 2 kPa) represent the dry season. Bottom: Relationship between the VPD and PAW per corresponding EC GPP values during the dry and growing seasons. The solid black line is the regression line with a 95% confidence interval in light gray shading.

Table 4. Summary of the partial correlation analysis between EC GPP, field, and Earth observation variables during the greening and browning phases. r_s is Spearman's Rho, t_s is the test statistic, and p is the significance of the test statistic.

Response = EC GPP	**Greening Phase** n **= 106**			**Browning Phase** n **= 75**		
	r_s	t_s	p	r_s	t_s	p
PAW	0.44	4.950	<0.01	0.16	0.156	0.18
VPD	−0.24	−2.525	0.01	−0.52	−0.523	<0.01
EVI	0.61	7.776	<0.05	0.60	6.289	<0.01
LST	−0.28	−2.957	<0.05	−0.34	−3.074	<0.01
BAND 7	0.32	3.426	<0.05	0.22	1.920	0.06

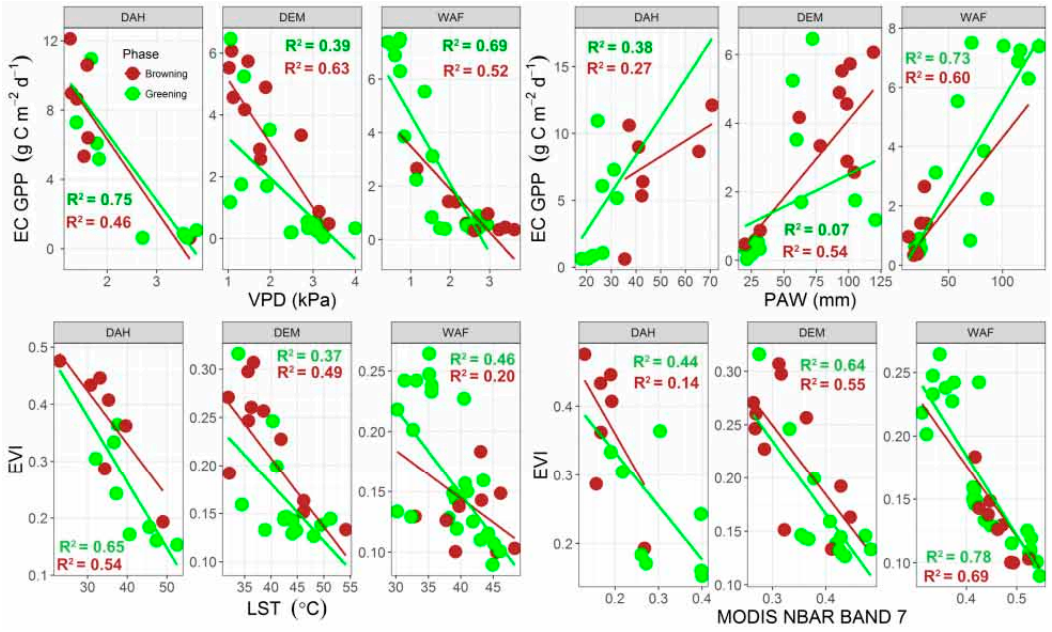

Figure 5. Scatterplots of the relationships between the field variables EC GPP, PAW and VPD (top row) and moderate-resolution imaging spectroradiometer (MODIS)-derived variables (bottom row) during the greening (green color) and browning (brown color) phases on a per-site basis. (DAH = Dahra, DEM = Demokeya, WAF = Wankama Fallow).

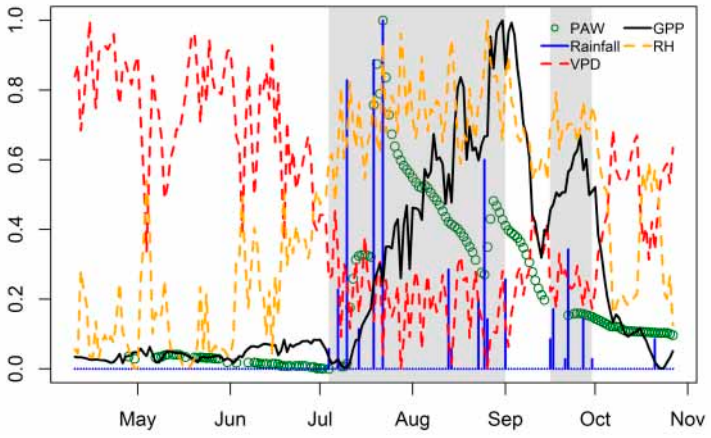

Figure 6. A narrowed-down example of a typical Sahelian growing season exemplified here by the 2009 growing season in Demokeya. Relative humidity (RH) begins to increase and vapor pressure deficit (VPD) begins to decrease a full month before the onset of the rainy season. Once the rains fall, plant-available water (PAW) is replenished and GPP begins to increase commencing the greening phase. Although PAW has been gradually decreasing during the growing season, the decrease in rainfall prompts a decrease in RH and an increase in VPD, which sharply reduced GPP due to stomatal closure. All variables have been normalized to between zero and one for visual purposes.

4.3. Eddy Covariance Gross Primary Productivity and MODIS-Derived Data

EVI was strongly correlated with EC GPP across all sites (R^2 = 0.83, RMSE = 1.04 g C m^{-2} d^{-1}) (Table 5). The partial correlation of the MODIS data showed that the EVI was closely coupled with EC GPP during both greening and browning phases (Table 4). The decline in PAW during the browning phase leads to a reduction in transpiration and latent heat flux and an increase in sensible heat flux and LST (r_s = −0.34) (Table 4, Figure 5). MODIS NBAR Band 7 exhibits a positive response during the greening (r_s = 0.32) and browning phases (r_s = 0.22), probably due to the band's sensitivity to changes

in soil moisture during the wetting and drying phases. The relationship between EVI, LST, and MODIS NBAR Band 7 is shown in Figure 7. The slope of the regression line during the dry season ($\beta_1 = -0.24$) shows a rapid increase in MODIS NBAR Band 7 for each unit decrease in EVI, whereas the change is more gradual during the growing season (Figure 7). Both MODIS NBAR Band 7 ($0.20 < R^2 < 0.50$) and LST ($0.33 < R^2 < 0.58$) had generally moderate relationships with EC GPP. However, when LST and MODIS NBAR Band 7 were included in an MLR model together with EVI, the combination was able to consistently explain higher variance ($R^2 \geq 0.88$) across all sites (Figure 8).

Both EVI and MLR GPP follow the seasonal progression of EC GPP well, but the MLR GPP model tracks the dry season EC GPP better than EVI (Figure 9). The inclusion of LST and MODIS NBAR Band 7 improves the variance explained by 6.7% from 0.83 for EVI to 0.89 for the MLR model comprising EVI, LST and MODIS NBAR Band 7 while decreasing the BIC from 1221 to 1024 (Table 5). When the data is split into the individual sites, a similar pattern emerges with the explained variance of MLR model over EVI increasing between 4.3% in Demokeya to 15.9% in Wankama (Table 5). The MLR GPP model for all the sites is shown in Equation (9):

$$GPP = -4.28 + [(34.51 \times EVI) + (-0.06 \times LST) + (7.81 \times BAND7)] \quad (9)$$

Table 5. Summary of the regression analysis between EC GPP and four Earth observation variables: enhanced vegetation index (EVI), land surface temperature (LST), MOD17 production efficiency model (MOD17 GPP), and MODIS NBAR Band 7 (BAND7) for each site. Also shown are the root-mean-square error (RMSE) and Bayesian information criterion (BIC) for each model.

Response = EC GPP			**Statistics**	
Demokeya	**RMSE**	**R^2**	***n***	**BIC**
BAND 7	1.70	0.20	97	392.13
LST	1.44	0.40	94	349.51
EVI	0.60	0.89	97	184.09
MOD17 GPP	0.89	0.77	95	262.10
EVI + LST	0.58	0.89	94	180.95
EVI + BAND 7	0.51	0.93	97	161.24
EVI + BAND7 + LST	0.48	0.93	94	155.54
Wankama Fallow	**RMSE**	**R^2**	***n***	**BIC**
LST	1.55	0.33	155	592.58
BAND 7	1.36	0.50	158	559.78
EVI	0.96	0.74	158	450.78
MOD17 GPP	1.43	0.44	123	452.12
EVI + LST	0.94	0.76	154	444.33
EVI + BAND 7	0.90	0.78	158	435.56
EVI + BAND7 + LST	0.67	0.88	154	344.91
Dahra	**RMSE**	**R^2**	***n***	**BIC**
BAND 7	2.73	0.38	156	772.01
LST	2.35	0.58	163	747.90
EVI	1.00	0.91	156	459.54
MOD17 GPP	1.35	0.86	166	587.48
EVI + LST	0.96	0.92	153	442.79
EVI + BAND 7	0.93	0.93	156	440.53
EVI + BAND7 + LST	0.85	0.96	153	414.90
All Sites	**RMSE**	**R^2**	***n***	**BIC**
BAND 7	2.18	0.32	411	1826.60
LST	2.03	0.42	412	1767.47
EVI	1.04	0.83	411	1220.91
MOD17 GPP	1.39	0.76	384	1362.45
EVI + LST	0.96	0.86	401	1131.69
EVI + BAND 7	0.91	0.88	411	1112.77
EVI + BAND7 + LST	0.84	0.89	401	1023.90

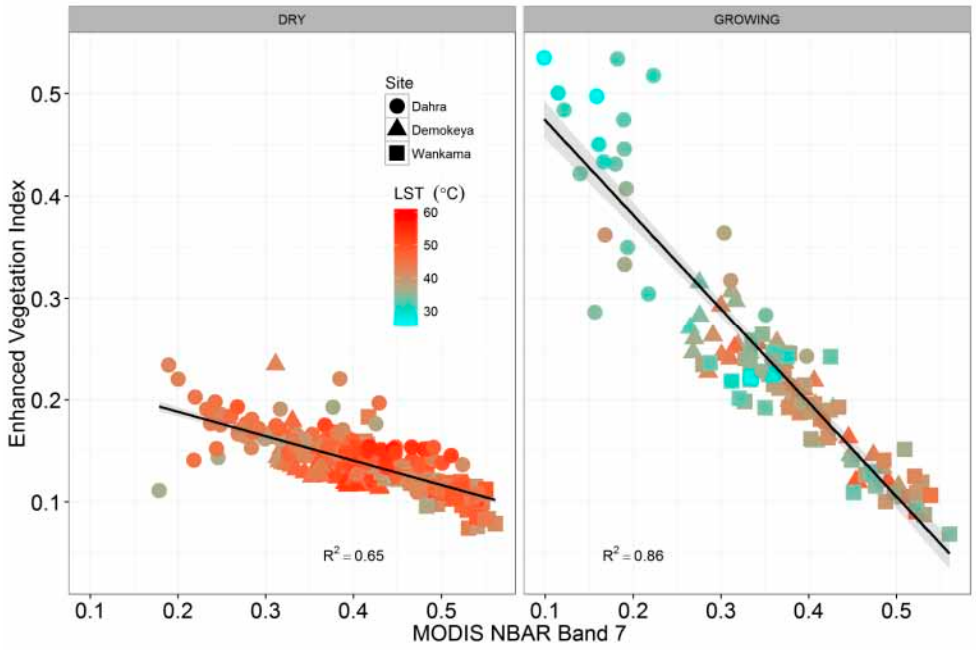

Figure 7. Comparison of EVI and MODIS NBAR Band 7, with coloring that indicates corresponding values of LST for each site during the growing (July–October) and dry season (November–June). The solid black line is the regression line with 95% confidence interval in light gray shading.

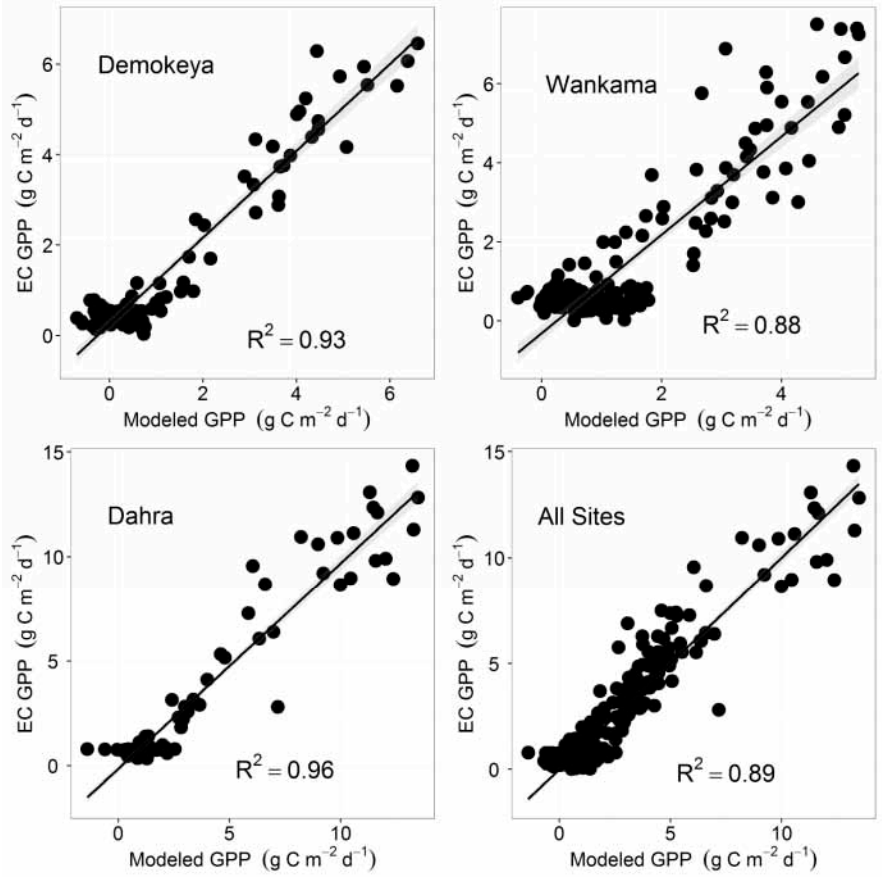

Figure 8. Cross-site relationship between the multiple linear regression (MLR) GPP model (~EVI + Band 7 + LST) and 8-day EC GPP for both the growing and seasons. The solid black line is the regression line with 95% confidence interval in light gray shading.

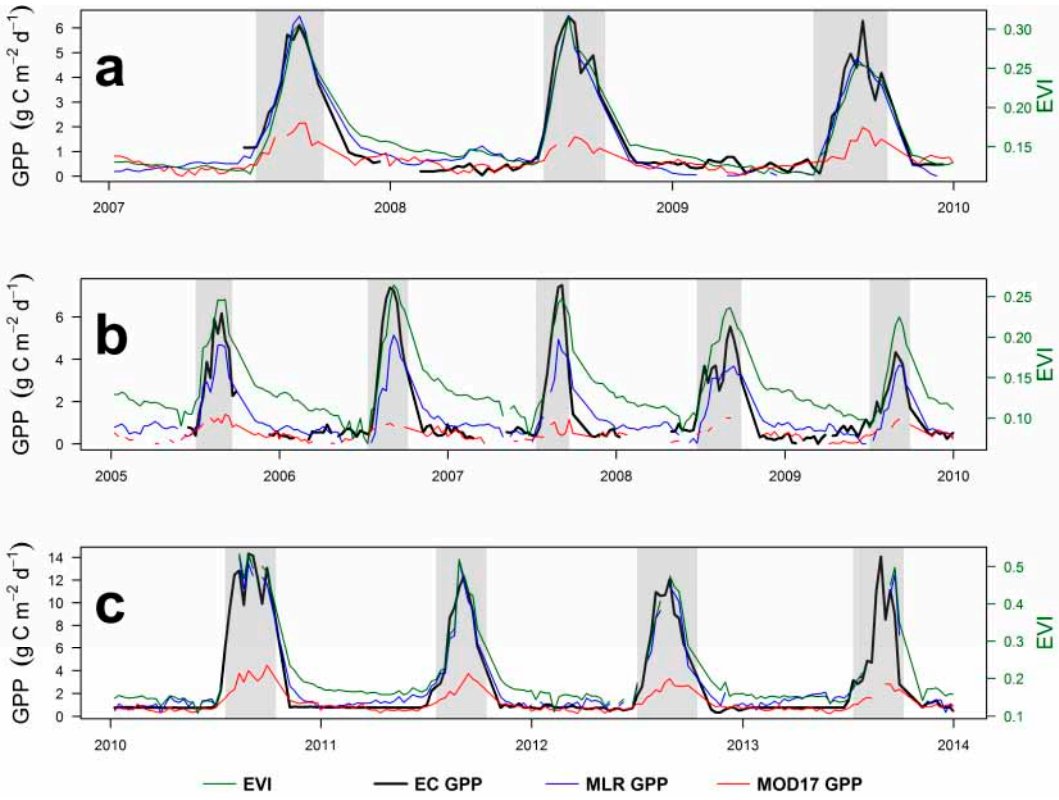

Figure 9. Cross-site comparison of 8-day EC GPP, EVI, the MLR GPP model, and MOD17 GPP for (**a**) Demokeya, (**b**) Wankama Fallow and (**c**) Dahra. The shading indicates the growing season (July–October). The large underestimation displayed by MOD17 GPP is due to the low value assigned to the maximum light use efficiency in the MOD17 algorithm [30].

The ability of the MLR model to explain cross-site variability in EC GPP was improved (from 85% to 89%) when data from both the growing and dry seasons were included in the model. Although, there is no green herbaceous vegetation during the dry season, the small C fluxes that were observed could be due to the sparse tree cover [36]. It is reasonable to assume that the dry season signal contains information about land memory effects [81,82]. However, it is unlikely that such effects would be passed on through soil moisture since upper layer dries out within two months of the start of the dry season [69]. Thus, such a memory could be retained in the dormant seeds, roots and foliage [68,83].

The spectral range of MODIS NBAR Band 7 is most sensitive to surface soil water content in general, and the rate of evaporation during the dry season in particular [35]. This is discernible in the relatively rapid increase of the surface reflectance of MODIS NBAR Band 7 compared to the decrease in EVI in response to the decline of the vegetative cover during the dry season (Figure 7). On the other hand, LST is linked to VPD due to the feedback between land (vegetated or bare) and near-surface air [49]. This is clearly shown in the relationship between EVI and LST during both the greening and browning phases in Figure 5. There have been other recent attempts to model GPP in water limited regions using EVI combined with other variables. For example, in a tropical xeric savanna ecosystem, Ma et al. [84] were able to explain 88% of the variability in EC GPP by parameterizing ecosystem light use efficiency using MODIS EVI and top-of-atmosphere photosynthetically active radiation. In another study, Sjöström et al. [21] found that the combination of MODIS EVI with flux tower-derived evaporative fraction, as a proxy of water availability, and photosynthetically active radiation significantly improved the modeling of EC GPP for seven African sites, including Demokeya and Wankama Fallow, with up to 73% of the variance explained. Using only Earth observation data, our model is able to explain 89% of the variance in EC GPP across the three Sahelian sites.

5. Conclusions

Hydrological processes generally control vegetation dynamics at multiple spatial and temporal scales. This is particularly true for the Sahel, where the short unimodal rainy season induces a net CO_2 uptake that is driven mainly by the herbaceous canopy [13]. Except in highly humid environments, all plants undergo photosynthesis at the expense of losing moisture to the atmosphere. This moisture loss is particularly significant for dryland vegetation, where an imbalance can occur between the amount of water plants require and the limited amount that is available in the ecosystem. In this study, we found that the two main moisture-related biophysical limitations, PAW and VPD together control plant CO_2 uptake in the semi-arid conditions. With the start of the dry season in November, low PAW is present in the drying soils of the Sahel, which leads to decreased availability of water for uptake by plant roots (Figures 3 and 4). This, in turn, reduces evapotranspiration (latent heat) due to drier soils and plants close their stomata to prevent moisture loss.

Considering both the importance of drylands in the global C cycle [85] and the dependence of human livelihoods on the products of photosynthesis [8], it is essential to account for water stress controls in order to better model primary productivity in this region. This is particularly important considering the fact that there is a chronic lack of field data on C fluxes in the Sahel. We found that the combination of MODIS NBAR Band 7 as a proxy for soil moisture variability, LST as a proxy for VPD, and EVI as a proxy of photosynthetic activity in an MLR model was able to explain 89% of the variability of EC GPP across the three Sahelian sites (Figures 8 and 9). Since EVI, LST, and MODIS NBAR Band 7 are based on Earth observation data, the MLR model presented here is potentially scalable with repeatable estimates of GPP at relatively high spatial and temporal resolutions. Moreover, the availability of standardized EC flux measurements, such as the recently released FLUXNET2015 database, can potentially eliminate variability in systematic and processing-induced uncertainties between sites. This can further improve model estimates when relating EC GPP with Earth observation data. Studies of the C cycle often focus on the growing season as it is the principal period where C assimilation takes place, however, the inclusion of dry season dynamics can potentially improve the explanatory capacity of GPP models by accounting for land memory effects. Further evaluation of this approach using more dryland sites from the FLUXNET2015 database as well as other types of in-situ validation data is required to test its efficiency in modeling GPP in water-limited areas.

Acknowledgments: Abdulhakim M. Abdi received support from the Lund University Center for Studies of Carbon Cycle and Climate Interactions (LUCCI) and the Royal Physiographic Society in Lund. Data for the Wankama (Niger) site were produced through the AMMA-CATCH regional observatory, funded by the French IRD and INSU national research institutes. Funding for this study was provided by the Swedish National Space Board (contract No. 100/11 to Jonas Ardö). The authors would like to thank all three reviewers of this manuscript for providing thoughtful and helpful comments.

Author Contributions: Abdulhakim M. Abdi conceived and designed the study, conducted the analysis, interpreted the results, and drafted the paper. Jonas Ardö, David E. Tenenbaum and Torbern Tagesson assisted with the study design and the interpretation of the results. Niklas Boke-Olén contributed to the analysis and the interpretation of the results. Bernard Cappelaere provided site data for Wankama and approved the final draft. All authors discussed the results and revised the manuscript.

Conflicts of Interest: The authors declare no conflict of interest.

References

1. Ellis, J.; Galvin, K.A. Climate patterns and land-use practices in the dry zones of Africa. *BioScience* **1994**, *44*, 340–349. [CrossRef]
2. Eklundh, L.; Olsson, L. Vegetation index trends for the African Sahel 1982–1999. *Geophys. Res. Lett.* **2003**, *30*, 1430. [CrossRef]
3. Olsson, L.; Eklundh, L.; Ardö, J. A recent greening of the Sahel—Trends, patterns and potential causes. *J. Arid Environ.* **2005**, *63*, 556–566. [CrossRef]
4. Dardel, C.; Kergoat, L.; Hiernaux, P.; Mougin, E.; Grippa, M.; Tucker, C.J. Re-greening Sahel: 30 years of remote sensing data and field observations (Mali, Niger). *Remote Sens. Environ.* **2014**, *140*, 350–364. [CrossRef]

5. Brandt, M.; Mbow, C.; Diouf, A.A.; Verger, A.; Samimi, C.; Fensholt, R. Ground- and satellite-based evidence of the biophysical mechanisms behind the greening Sahel. *Glob. Chang. Biol.* **2015**, *21*, 1610–1620. [CrossRef] [PubMed]
6. Seaquist, J.; Olsson, L.; Ardö, J.; Eklundh, L. Broad-scale increase in NPP quantified for the African Sahel, 1982–1999. *Int. J. Remote Sens.* **2006**, *27*, 5115–5122. [CrossRef]
7. Hickler, T.; Eklundh, L.; Seaquist, J.W.; Smith, B.; Ardö, J.; Olsson, L.; Sykes, M.T.; Sjöström, M. Precipitation controls Sahel greening trend. *Geophys. Res. Lett.* **2005**, *32*, L21415. [CrossRef]
8. Abdi, A.M.; Seaquist, J.; Tenenbaum, D.E.; Eklundh, L.; Ardo, J. The supply and demand of net primary production in the Sahel. *Environ. Res. Lett.* **2014**, *9*, 094003. [CrossRef]
9. Vrieling, A.; de Leeuw, J.; Said, M. Length of growing period over Africa: Variability and trends from 30 years of NDVI time series. *Remote Sens.* **2013**, *5*, 982–1000. [CrossRef]
10. Philippon, N.; Martiny, N.; Camberlin, P.; Hoffman, M.T.; Gond, V. Timing and patterns of the ENSO signal in Africa over the last 30 years: Insights from normalized difference vegetation index data. *J. Clim.* **2014**, *27*, 2509–2532. [CrossRef]
11. Nicholson, S.E. *Dryland Climatology*; Cambridge University Press: Cambridge, UK, 2011.
12. Le Houérou, H.N. Definition, geographical limits, contacts with other ecoclimatic zones. In *The Grazing Land Ecosystems of the African Sahel*; Springer: Berlin/Heidelberg, Germany, 1989; pp. 1–16.
13. Tagesson, T.; Fensholt, R.; Cappelaere, B.; Mougin, E.; Horion, S.; Kergoat, L.; Nieto, H.; Mbow, C.; Ehammer, A.; Demarty, J.; et al. Spatiotemporal variability in carbon exchange fluxes across the Sahel. *Agric. For. Meteorol.* **2016**, *226*, 108–118. [CrossRef]
14. Hiernaux, P.; Le Houérou, H.N. Les parcours du Sahel. *Sci. Chang. Planét/Sécheresse* **2006**, *17*, 51–71.
15. Brandt, M.; Hiernaux, P.; Rasmussen, K.; Mbow, C.; Kergoat, L.; Tagesson, T.; Ibrahim, Y.Z.; Wélé, A.; Tucker, C.J.; Fensholt, R. Assessing woody vegetation trends in Sahelian drylands using MODIS based seasonal metrics. *Remote Sens. Environ.* **2016**, *183*, 215–225. [CrossRef]
16. Tucker, C.J.; Vanpraet, C.; Boerwinkel, E.; Gaston, A. Satellite remote sensing of total dry matter production in the Senegalese Sahel. *Remote Sens. Environ.* **1983**, *13*, 461–474. [CrossRef]
17. Prince, S.D. Satellite remote sensing of primary production: Comparison of results for Sahelian grasslands 1981–1988. *Int. J. Remote Sens.* **1991**, *12*, 1301–1311. [CrossRef]
18. Verhoef, A.; Allen, S.J.; Bruin, H.A.R.; Jacobs, C.M.J.; Heusinkveld, B.G. Fluxes of carbon dioxide and water vapour from a Sahelian savanna. *Agric. For. Meteorol.* **1996**, *80*, 231–248. [CrossRef]
19. Moncrieff, J.B.; Monteny, B.; Verhoef, A.; Friborg, T.; Elbers, J.; Kabat, P.; de Bruin, H.; Soegaard, H.; Jarvis, P.G.; Taupin, J.D. Spatial and temporal variations in net carbon flux during HAPEX-Sahel. *J. Hydrol.* **1997**, *188*, 563–588. [CrossRef]
20. Nicholson, S.E.; Tucker, C.J.; Ba, M. Desertification, drought, and surface vegetation: An example from the West African Sahel. *Bull. Am. Meteorol. Soc.* **1998**, *79*, 815–830. [CrossRef]
21. Sjöström, M.; Ardö, J.; Arneth, A.; Boulain, N.; Cappelaere, B.; Eklundh, L.; De Grandcourt, A.; Kutsch, W.; Merbold, L.; Nouvellon, Y. Exploring the potential of MODIS EVI for modeling gross primary production across African ecosystems. *Remote Sens. Environ.* **2011**, *115*, 1081–1089. [CrossRef]
22. Merbold, L.; Ardö, J.; Arneth, A.; Scholes, R.; Nouvellon, Y.; De Grandcourt, A.; Archibald, S.; Bonnefond, J.; Boulain, N.; Brueggemann, N. Precipitation as driver of carbon fluxes in 11 African ecosystems. *Biogeosciences* **2009**, *6*, 1027–1041. [CrossRef]
23. Nutini, F.; Boschetti, M.; Candiani, G.; Bocchi, S.; Brivio, P. Evaporative fraction as an indicator of moisture condition and water stress status in semi-arid rangeland ecosystems. *Remote Sens.* **2014**, *6*, 6300. [CrossRef]
24. Velluet, C.; Demarty, J.; Cappelaere, B.; Braud, I.; Issoufou, H.B.A.; Boulain, N.; Ramier, D.; Mainassara, I.; Charvet, G.; Boucher, M.; et al. Building a field- and model-based climatology of local water and energy cycles in the cultivated Sahel—Annual budgets and seasonality. *Hydrol. Earth Syst. Sci.* **2014**, *18*, 5001–5024. [CrossRef]
25. Boegh, E.; Soegaard, H.; Hanan, N.; Kabat, P.; Lesch, L. A Remote sensing study of the NDVI-Ts relationship and the transpiration from sparse vegetation in the sahel based on high-resolution satellite data. *Remote Sens. Environ.* **1999**, *69*, 224–240. [CrossRef]
26. Ago, E.E.; Serça, D.; Agbossou, E.K.; Galle, S.; Aubinet, M. Carbon dioxide fluxes from a degraded woodland in West Africa and their responses to main environmental factors. *Carbon Balance Manag.* **2015**, *10*, 22. [CrossRef] [PubMed]

27. Ardö, J. Increasing the confidence of African carbon cycle assessments. In Proceedings of the EGU General Assembly 2016, Vienna, Austria, 17–22 April 2016.
28. Running, S.W.; Thornton, P.E.; Nemani, R.R.; Glassy, J.M. Global terrestrial gross and net primary productivity from the Earth Observing System. In *Methods in Ecosystem Science*; Sala, O.E., Mooney, H.A., Howarth, R.W., Eds.; Springer: New York, NY, USA, 2000; pp. 44–57.
29. Monteith, J.L. Solar radiation and productivity in tropical ecosystems. *J. Appl. Ecol.* **1972**, *9*, 747–766. [CrossRef]
30. Sjöström, M.; Zhao, M.; Archibald, S.; Arneth, A.; Cappelaere, B.; Falk, U.; de Grandcourt, A.; Hanan, N.; Kergoat, L.; Kutsch, W.; et al. Evaluation of MODIS gross primary productivity for Africa using eddy covariance data. *Remote Sens. Environ.* **2013**, *131*, 275–286. [CrossRef]
31. Sadeghi, M.; Jones, S.B.; Philpot, W.D. A linear physically-based model for remote sensing of soil moisture using short wave infrared bands. *Remote Sens. Environ.* **2015**, *164*, 66–76. [CrossRef]
32. Liang, S.; Zhong, B.; Fang, H. Improved estimation of aerosol optical depth from MODIS imagery over land surfaces. *Remote Sens. Environ.* **2006**, *104*, 416–425. [CrossRef]
33. Lobell, D.B.; Asner, G.P. Moisture Effects on Soil Reflectance. *Soil Sci. Soc. Am. J.* **2002**, *66*, 722–727. [CrossRef]
34. Weidong, L.; Baret, F.; Xingfa, G.; Qingxi, T.; Lanfen, Z.; Bing, Z. Relating soil surface moisture to reflectance. *Remote Sens. Environ.* **2002**, *81*, 238–246. [CrossRef]
35. Tian, J.; Philpot, W.D. Relationship between surface soil water content, evaporation rate, and water absorption band depths in SWIR reflectance spectra. *Remote Sens. Environ.* **2015**, *169*, 280–289. [CrossRef]
36. Ardö, J.; Molder, M.; El-Tahir, B.A.; Elkhidir, H.A. Seasonal variation of carbon fluxes in a sparse savanna in semi arid Sudan. *Carbon Balance Manag.* **2008**, *3*, 7. [CrossRef] [PubMed]
37. Cappelaere, B.; Descroix, L.; Lebel, T.; Boulain, N.; Ramier, D.; Laurent, J.P.; Favreau, G.; Boubkraoui, S.; Boucher, M.; Bouzou Moussa, I.; et al. The AMMA-CATCH experiment in the cultivated Sahelian area of south-west Niger—Investigating water cycle response to a fluctuating climate and changing environment. *J. Hydrol.* **2009**, *375*, 34–51. [CrossRef]
38. Tagesson, T.; Fensholt, R.; Guiro, I.; Rasmussen, M.O.; Huber, S.; Mbow, C.; Garcia, M.; Horion, S.; Sandholt, I.; Holm-Rasmussen, B.; et al. Ecosystem properties of semiarid savanna grassland in West Africa and its relationship with environmental variability. *Glob. Chang. Biol.* **2015**, *21*, 250–264. [CrossRef] [PubMed]
39. Olsson, L.; Ardö, J. Soil carbon sequestration in degraded semiarid agro-ecosystems-perils and potentials. *AMBIO J. Hum. Environ.* **2002**, *31*, 471–477. [CrossRef]
40. Boulain, N.; Cappelaere, B.; Ramier, D.; Issoufou, H.B.A.; Halilou, O.; Seghieri, J.; Guillemin, F.; Oï, M.; Gignoux, J.; Timouk, F. Towards an understanding of coupled physical and biological processes in the cultivated Sahel—2. Vegetation and carbon dynamics. *J. Hydrol.* **2009**, *375*, 190–203. [CrossRef]
41. Tagesson, T.; Fensholt, R.; Cropley, F.; Guiro, I.; Horion, S.; Ehammer, A.; Ardö, J. Dynamics in carbon exchange fluxes for a grazed semi-arid savanna ecosystem in West Africa. *Agric. Ecosyst. Environ.* **2015**, *205*, 15–24. [CrossRef]
42. Schaaf, C.B.; Gao, F.; Strahler, A.H.; Lucht, W.; Li, X.; Tsang, T.; Strugnell, N.C.; Zhang, X.; Jin, Y.; Muller, J.-P.; et al. First operational BRDF, albedo nadir reflectance products from MODIS. *Remote Sens. Environ.* **2002**, *83*, 135–148. [CrossRef]
43. Sjöström, M.; Ardö, J.; Eklundh, L.; El-Tahir, B.; El-Khidir, H.; Hellström, M.; Pilesjö, P.; Seaquist, J. Evaluation of satellite based indices for gross primary production estimates in a sparse savanna in the Sudan. *Biogeosciences* **2009**, *6*, 129–138. [CrossRef]
44. Tagesson, T.; Fensholt, R.; Huber, S.; Horion, S.; Guiro, I.; Ehammer, A.; Ardö, J. Deriving seasonal dynamics in ecosystem properties of semi-arid savanna grasslands from in situ-based hyperspectral reflectance. *Biogeosciences* **2015**, *12*, 4621–4635. [CrossRef]
45. Vancutsem, C.; Ceccato, P.; Dinku, T.; Connor, S.J. Evaluation of MODIS land surface temperature data to estimate air temperature in different ecosystems over Africa. *Remote Sens. Environ.* **2010**, *114*, 449–465. [CrossRef]
46. Jägermeyr, J.; Gerten, D.; Lucht, W.; Hostert, P.; Migliavacca, M.; Nemani, R. A high-resolution approach to estimating ecosystem respiration at continental scales using operational satellite data. *Glob. Chang. Biol.* **2014**, *20*, 1191–1210. [CrossRef] [PubMed]

47. Hashimoto, H.; Dungan, J.L.; White, M.A.; Yang, F.; Michaelis, A.R.; Running, S.W.; Nemani, R.R. Satellite-based estimation of surface vapor pressure deficits using MODIS land surface temperature data. *Remote Sens. Environ.* **2008**, *112*, 142–155. [CrossRef]
48. Sims, D.A.; Rahman, A.F.; Cordova, V.D.; El-Masri, B.Z.; Baldocchi, D.D.; Bolstad, P.V.; Flanagan, L.B.; Goldstein, A.H.; Hollinger, D.Y.; Misson, L.; et al. A new model of gross primary productivity for North American ecosystems based solely on the enhanced vegetation index and land surface temperature from MODIS. *Remote Sens. Environ.* **2008**, *112*, 1633–1646. [CrossRef]
49. Pappas, C.; Fatichi, S.; Leuzinger, S.; Wolf, A.; Burlando, P. Sensitivity analysis of a process-based ecosystem model: Pinpointing parameterization and structural issues. *J. Geophys. Res. Biogeosci.* **2013**, *118*, 505–528. [CrossRef]
50. Zotarelli, L.; Dukes, M.D.; Morgan, K.T. *Interpretation of Soil Moisture Content to Determine Soil Field Capacity and Avoid Over-Irrigating Sandy Soils Using Soil Moisture Sensors*; UF/IFAS Extension: Gainesville, FL, USA, 2010.
51. Dorigo, W.A.; Wagner, W.; Hohensinn, R.; Hahn, S.; Paulik, C.; Xaver, A.; Gruber, A.; Drusch, M.; Mecklenburg, S.; van Oevelen, P.; et al. The International Soil Moisture Network: A data hosting facility for global in situ soil moisture measurements. *Hydrol. Earth Syst. Sci.* **2011**, *15*, 1675–1698. [CrossRef]
52. Leenaars, J.; van Oostrum, A.; Ruiperez Gonzalez, M. *Africa Soil Profiles Database, Version 1.2. A Compilation of Geo-Referenced and Standardised Legacy Soil Profile Data for Sub-Saharan Africa (with Dataset)*; ISRIC—World Soil Information: Wageningen, The Netherlands, 2014.
53. Dingman, S.L. *Physical Hydrology*, 3rd ed.; Waveland Press: Long Grove, IL, USA, 2015.
54. Anderson, D.B. Relative humidity or vapor pressure deficit. *Ecology* **1936**, *17*, 277–282. [CrossRef]
55. Maroco, J.P.; Pereira, J.S.; Chaves, M.M. Stomatal responses to leaf-to-air vapour pressure deficit in sahelian species. *Funct. Plant Biol.* **1997**, *24*, 381–387. [CrossRef]
56. Ward, A.D.; Trimble, S.W.; Burckhard, S.R.; Lyon, J.G. *Environmental Hydrology*, 3rd ed.; CRC Press: Boca Raton, FL, USA, 2015.
57. Kohler, M.; Linsley, R. *Predicting the Runoff from Storm Rainfall*; National Oceanic and Atmospheric Administration: Washington, DC, USA, 1951.
58. Choudhury, B.J.; Golus, R.E. Estimating soil wetness using satellite data. *Int. J. Remote Sens.* **1988**, *9*, 1251–1257. [CrossRef]
59. Heggen, R.J. Normalized Antecedent Precipitation Index. *J. Hydrol. Eng.* **2001**, *6*, 377–381. [CrossRef]
60. Hong, Y.; Adler, R.F.; Hossain, F.; Curtis, S.; Huffman, G.J. A first approach to global runoff simulation using satellite rainfall estimation. *Water Resour. Res.* **2007**, *43*, W08502. [CrossRef]
61. Gao, X.; Huete, A.R.; Ni, W.; Miura, T. Optical–biophysical relationships of vegetation spectra without background contamination. *Remote Sens. Environ.* **2000**, *74*, 609–620. [CrossRef]
62. Huete, A.; Didan, K.; Miura, T.; Rodriguez, E.P.; Gao, X.; Ferreira, L.G. Overview of the radiometric and biophysical performance of the MODIS vegetation indices. *Remote Sens. Environ.* **2002**, *83*, 195–213. [CrossRef]
63. Ma, X.; Huete, A.; Yu, Q.; Coupe, N.R.; Davies, K.; Broich, M.; Ratana, P.; Beringer, J.; Hutley, L.B.; Cleverly, J.; et al. Spatial patterns and temporal dynamics in savanna vegetation phenology across the North Australian Tropical Transect. *Remote Sens. Environ.* **2013**, *139*, 97–115. [CrossRef]
64. Spearman, C. The proof and measurement of association between two things. *Am. J. Psychol.* **1904**, *15*, 72–101. [CrossRef]
65. Schwarz, G. Estimating the dimension of a model. *Ann. Stat.* **1978**, *6*, 461–464. [CrossRef]
66. Zhao, W.; Ji, X. Spatio-temporal variation in transpiration responses of maize plants to vapor pressure deficit under an arid climatic condition. *J. Arid Land* **2016**, *8*, 409–421. [CrossRef]
67. Kutsch, W.L.; Hanan, N.; Scholes, B.; McHugh, I.; Kubheka, W.; Eckhardt, H.; Williams, C. Response of carbon fluxes to water relations in a savanna ecosystem in South Africa. *Biogeosciences* **2008**, *5*, 1797–1808. [CrossRef]
68. Schwinning, S.; Sala, O.E.; Loik, M.E.; Ehleringer, J.R. Thresholds, memory, and seasonality: Understanding pulse dynamics in arid/semi-arid ecosystems. *Oecologia* **2004**, *141*, 191–193. [CrossRef] [PubMed]
69. Shinoda, M.; Yamaguchi, Y. Influence of soil moisture anomaly on temperature in the Sahel: A Comparison between wet and dry decades. *J. Hydrometeorol.* **2003**, *4*, 437–447. [CrossRef]
70. Tagesson, T.; Ardö, J.; Guiro, I.; Cropley, F.; Mbow, C.; Horion, S.; Ehammer, A.; Mougin, E.; Delon, C.; Galy-Lacaux, C.; et al. Very high CO_2 exchange fluxes at the peak of the rainy season in a West African grazed semi-arid savanna ecosystem. *Geograf. Tidsskr. Dan. J. Geogr.* **2016**, *116*, 93–109. [CrossRef]

71. Steiner, A.L.; Pal, J.S.; Rauscher, S.A.; Bell, J.L.; Diffenbaugh, N.S.; Boone, A.; Sloan, L.C.; Giorgi, F. Land surface coupling in regional climate simulations of the West African monsoon. *Clim. Dyn.* **2009**, *33*, 869–892. [CrossRef]
72. Sultan, B.; Janicot, S.; Diedhiou, A. The West African Monsoon Dynamics. Part I: Documentation of Intraseasonal Variability. *J. Clim.* **2003**, *16*, 3389–3406. [CrossRef]
73. Browne, N.A.K.; Sylla, M.B. Regional climate model sensitivity to domain size for the simulation of the West African summer monsoon rainfall. *Int. J. Geophys.* **2012**, *2012*, 1–17. [CrossRef]
74. Messager, C.; Gallée, H.; Brasseur, O. Precipitation sensitivity to regional SST in a regional climate simulation during the West African monsoon for two dry years. *Clim. Dyn.* **2004**, *22*, 249–266. [CrossRef]
75. Gargallo-Garriga, A.; Sardans, J.; Pérez-Trujillo, M.; Rivas-Ubach, A.; Oravec, M.; Vecerova, K.; Urban, O.; Jentsch, A.; Kreyling, J.; Beierkuhnlein, C.; et al. Opposite metabolic responses of shoots and roots to drought. *Sci. Rep.* **2014**, *4*, 6829. [CrossRef] [PubMed]
76. Otieno, D.O.; K'Otuto, G.O.; Maina, J.N.; Kuzyakov, Y.; Onyango, J.C. Responses of ecosystem carbon dioxide fluxes to soil moisture fluctuations in a moist Kenyan savanna. *J. Trop. Ecol.* **2010**, *26*, 605–618. [CrossRef]
77. Hasibeder, R.; Fuchslueger, L.; Richter, A.; Bahn, M. Summer drought alters carbon allocation to roots and root respiration in mountain grassland. *New Phytol.* **2015**, *205*, 1117–1127. [CrossRef] [PubMed]
78. Murray-Tortarolo, G.; Friedlingstein, P.; Sitch, S.; Seneviratne, S.I.; Fletcher, I.; Mueller, B.; Greve, P.; Anav, A.; Liu, Y.; Ahlström, A.; et al. The dry season intensity as a key driver of NPP trends. *Geophys. Res. Lett.* **2016**, *43*, 2632–2639. [CrossRef]
79. Ardö, J.; Olsson, L. Soil carbon sequestration in traditional farming in sudanese dry lands. *Environ. Manag.* **2004**, *33*, S318–S329. [CrossRef]
80. De Bie, S.; Ketner, P.; Paasse, M.; Geerling, C. Woody plant phenology in the West Africa savanna. *J. Biogeogr.* **1998**, *25*, 883–900. [CrossRef]
81. Fontaine, B.; Louvet, S.; Roucou, P. Fluctuations in annual cycles and inter-seasonal memory in West Africa: Rainfall, soil moisture and heat fluxes. *Theor. Appl. Climatol.* **2007**, *88*, 57–70. [CrossRef]
82. Dirmeyer, P.A.; Schlosser, C.A.; Brubaker, K.L. Precipitation, recycling, and land memory: An integrated analysis. *J. Hydrometeorol.* **2009**, *10*, 278–288. [CrossRef]
83. Hiernaux, P.; Cissé, M.; Diarra, L.; De Leeuw, P. Fluctuations saisonnières de la feuillaison des arbres et des buissons sahéliens. Conséquences pour la quantification des ressources fourragères. *Revue D'élevage Médecine Vétérinaire Des Pays Tropicaux* **1994**, *47*, 117–125.
84. Ma, X.; Huete, A.; Yu, Q.; Restrepo-Coupe, N.; Beringer, J.; Hutley, L.B.; Kanniah, K.D.; Cleverly, J.; Eamus, D. Parameterization of an ecosystem light-use-efficiency model for predicting savanna GPP using MODIS EVI. *Remote Sens. Environ.* **2014**, *154*, 253–271. [CrossRef]
85. Ahlström, A.; Raupach, M.R.; Schurgers, G.; Smith, B.; Arneth, A.; Jung, M.; Reichstein, M.; Canadell, J.G.; Friedlingstein, P.; Jain, A.K.; et al. The dominant role of semi-arid ecosystems in the trend and variability of the land CO_2 sink. *Science* **2015**, *348*, 895–899. [CrossRef] [PubMed]